Title

Performance comparison of dual-ended readout depth-encoding PET detectors based on BGO and LYSO crystals

Journal

Physics in Medicine and Biology, 65(23)

ISSN

0031-9155

Authors

Du, Junwei
Ariño-Estrada, Gerard
Bai, Xiaowei
et al.

Publication Date

2020-12-07

DOI

10.1088/1361-6560/abc365

Peer reviewed

HHS Public Access

Author manuscript

Phys Med Biol. Author manuscript; available in PMC 2022 February 03.

Published in final edited form as:

Phys Med Biol. ; 65(23): . doi:10.1088/1361-6560/abc365.

Performance comparison of dual-ended readout depth-encoding PET detectors based on BGO and LYSO crystals

Junwei Du, **Gerard Ariño-Estrada**, **Xiaowei Bai**, **Simon R Cherry**

Department of Biomedical Engineering, University of California at Davis, One Shields Avenue, Davis, CA 95616, United States of America

Abstract

The performance of dual-ended readout depth-encoding positron emission tomography (PET) detectors based on bismuth germanate (BGO) coupled to silicon photomultipliers (SiPM) arrays was measured for the first time and compared to lutetium-yttrium oxyorthosilicate (LYSO)-based detectors using the same readout. The BGO and LYSO crystal arrays all had a crystal pitch of 2.2 mm and were coupled to 8 × 8 SiPM arrays with a matching pitch of 2.2 mm, using a one-to-one coupling configuration. Three types of crystals with Toray reflector were used: polished LYSO, polished BGO, and unpolished BGO, and for two different crystal thicknesses of 20 mm and 30 mm. All the crystal elements in the BGO arrays were clearly resolved in the flood histogram. Better flood histograms were obtained using the LYSO arrays for a selected crystal thickness, and better flood histograms were obtained using the 20 mm thick crystal arrays for a selected crystal type. The average crystal level energy resolution and timing resolution for 20 mm polished LYSO, polished BGO and unpolished BGO crystals at their optimal SiPM bias voltage were 18.6 ± 1.3% and 1.19 ± 0.20 ns, 17.8 ± 0.8% and 4.43 ± 0.47 ns, and 18.0 ± 1.0% and 4.68 ± 1.0 ns, respectively. Depth-of-interaction (DOI) resolution of the 20 mm polished LYSO array was 2.31 ± 0.17 mm and for the 20 mm unpolished BGO array was 3.53 ± 0.25 mm. However, polished BGO arrays with Toray reflector did not provide DOI information. Our key conclusion is that dual-ended readout depth-encoding 20 mm thick unpolished BGO detectors are good candidates for low-activity PET systems with small field-of-view and low timing performance requirements, such as preclinical or compact organ-dedicated PET systems, with the advantage over LYSO of having no background radiation and significantly lower cost.

Keywords

PET; DOI; BGO; LYSO

1. Introduction

Lutetium oxyorthosilicate (LSO), lutetium yttrium oxyorthosilicate (LYSO) and bismuth germanate (BGO) are the three most popular scintillators used in positron emission tomography (PET). LSO and LYSO have similar properties, and are today the preferred choice in state-of-the-art clinical time-of-flight (TOF) PET and pre-clinical PET scanners

jwdu@ucdavis.edu .

due to their high light output and fast decay time (Gundacker et al 2016, Yamamoto et al 2016, Cherry et al 2018, Akamatsu et al 2019, Conti and Bendriem 2019, Gsell et al 2020). Compared to L(Y)SO, BGO has lower light yield and slower decay time (table 1) (Ramirez et al 2005, de Marcillac et al 2003, Du et al 2009). However, BGO has higher effective atomic number (Z_{eff}) (table 1), and 35 times lower intrinsic radiation than L(Y)SO making it practically a background-free material (de Marcillac et al 2003, Zhang et al 2010), and has substantially lower production cost. The higher effective atomic number leads to a greater photoelectric cross section and increased detection efficiency of 511 keV photons, which helps to reduce inter-crystal scatter (Shao et al 1996), especially for crystal arrays with small crystal pitch size. Further, BGO-based PET scanners are expected to show better performance than L(Y)SO-based scanners in ultra-low activity studies, such as cell-tracking studies, where low radiation background is very important (Bao and Chatziioannou 2010, Freedenberg et al 2014, Ouyang et al 2016).

Good depth-of-interaction (DOI) information for both annihilation photons is essential in PET scanners to achieve uniform high spatial resolution across the whole field-of-view (FOV) (Shao et al 2014, St James et al 2014). Compared to other depth-encoding methods, such as multilayer crystals (Ito et al 2010, Gonzalez et al 2016b, Watanabe et al 2017, Akamatsu et al 2019), custom reflector designs (Zhang et al 2016, Son et al 2017, Kuang et al 2018, Pizzichemi et al 2019) and use of the scintillation light spread in monolithic crystals (González et al 2016a, Müller et al 2019), dual-ended readout using photodetectors coupled to both ends of the crystal array can provide excellent DOI information and very high spatial resolution at the same time (Du et al 2018, 2019b). Dual-ended readout PET detectors based on L(Y)SO arrays with different surface treatments and different reflectors have been extensively studied both using silicon photomultiplier (SiPM) and avalanche photodiode (APD) as photodetectors (Ren et al 2014, Yang et al 2019). Small-animal PET scanners with L(Y)SO-based dual-ended readout detectors have shown the spatial resolution across the FOV can be significantly improved by using the DOI information (Shao et al 2014, Yang et al 2016). However, to the best of our knowledge, the performance of dual-ended readout detectors based on BGO arrays has not been yet studied.

In this paper, the performance of dual-ended readout BGO-based PET detectors using SiPM arrays was compared to LYSO-based detectors with the same readout in terms of flood histogram quality, energy resolution, timing resolution and DOI resolution.

2. Detector and readout electronics

2.1. Dual-ended readout detector

Figure 1 shows the LYSO and BGO arrays used in this study. Details of the crystal arrays are provided in table 2. All the polished surfaces of the crystals were machine polished by the manufacturers. All the crystal arrays were arranged in an 8 × 8 element configuration with a pitch size of 2.2 mm, and thicknesses of 20 mm and 30 mm. Toray E60 (Toray Industries, Inc. Japan) with a thickness of 50 μm was used as the inter crystal reflector, and optical glue OP-30 (Dymax Corporation, USA) with a thickness of 5 μm was used to glue the reflector to the crystals.

S13361-2050-08 SiPM arrays (Hamamatsu Photonics K.K., Japan) were used as the photodetectors (figure 2 (left)). The S13361-2050-08 SiPM array consisted of an 8 × 8 SiPM configuration with a pitch size of 2.2 mm. Each SiPM pixel had an active area of 2×2 mm^2 and was fabricated using 50 μm microcells. The same four SiPM arrays were used for all the measurements. To keep the relative positions of the SiPM arrays and the scintillator arrays fixed in relation to each other, 3D printed holders were used, as shown in figure 2 (right). Optical grease BC-630 (Saint-Gobain Crystals, USA) was used as the optical coupling material between the SiPM arrays and the crystal arrays.

2.2. Readout electronics

A block schematic of the readout electronics for flood histogram and timing measurements is shown in figure 3. For each detector module, the 128 SiPM signals were amplified individually and then reduced to eight position signals (X_1^+, X_1^-, Y_1^+, Y_1^- and X_2^+, X_2^-, Y_2^+, Y_2^-) and one timing signal (from the sum of all the 128 amplified signals) using custom-designed amplifier boards (Du et al 2019a). The 16 position signals of the two detector modules were sent to a 16-channel shaping amplifier N568B (CAEN, Italy) and digitized using a 32-channel digitizer DT5740D (CAEN) at a speed of 62.5 megasamples per second (MSPS). The timing signals of the two detector modules were coupled to constant fraction discriminators (CFDs) model ORTEC 584 (ORTEC, USA) to generate the timing triggers. Each timing trigger was split into two branches, one branch was connected to a time-to-amplitude converter (TAC) (ORTEC 584) for timing resolution measurement and the other was connected to a coincidence module Model Phillips 768 (Phillips Scientific, USA) to select coincidence events on-line. The output of the TAC was also digitized by the DT 5740D digitizer, and the output of the coincidence module was used as a trigger for the digitizer. The output of the digitizer was sent to a computer for further processing.

3. Experimental methods

A 925 kBq (25 μCi) ^{22}Na point source with a diameter of 0.25 mm was used in all experiments and a 350–750 keV energy window was applied to each crystal to select coincidence events. The temperature inside the experimental enclosure was monitored and kept at 12.6 ± 0.2 °C by sending cold, dry air to the box.

3.1. Flood histogram

The flood histogram, energy resolution and timing resolution were measured using two identical detectors for each crystal material, array thickness, and polishing type. The distance between the two detectors was 150 mm and the ^{22}Na source was located in the center between the two detectors. Data for the flood histogram measurement, energy resolution and timing resolution were acquired as a function of SiPM bias voltage. The range of bias voltages tested ranged between 53.0–58.5 V for the LYSO-based detectors and 54.0 V–58.5 V for the BGO-based detectors. The bias voltage was incremented in steps of 0.5 V.

The gamma photon interaction position was calculated using the eight digitized position signals and equation (1),

$$x = \frac{1}{2}\left(\frac{X_1^+ - X_1^-}{X_1^+ + X_1^-} + \frac{X_2^+ - X_2^-}{X_2^+ + X_2^-}\right), y = \frac{1}{2}\left(\frac{Y_1^+ - Y_1^-}{Y_1^+ + Y_1^-} + \frac{Y_2^+ - Y_2^-}{Y_2^+ + Y_2^-}\right) \quad (1)$$

where X_i^+, X_i^- Y_i^+, Y_i^- ($i = 1, 2$) were the four position signals from SiPMs 1 and 2 coupled to both ends of the same crystal array.

To quantitatively compare the flood histograms obtained under different conditions, the flood histogram quality was evaluated by a flood histogram metric k, which was described in detail in (Du et al 2016) and was calculated using equation (2),

$$k = \frac{1}{64}\sum_{i=1}^{64} k_i,\ k_{\text{std}} = \sqrt{\frac{1}{63}\sum_{i=1}^{64}(k_i - k)^2} \quad (2)$$

where k_i ($i = 1,\ldots,64$) is the flood histogram metric for each crystal across the crystal array and calculated using the ratio of the distance to the width of the crystal spots in the flood histogram (Du et al 2016). k was the average value of k_i across all the 64 crystals in the LYSO array and was used to measure the flood histogram quality of the detector. The standard deviation k_{std} of all k_i was used as the error range of k. A larger value of k and a smaller value of k_{std} indicate better flood histogram quality (Du et al 2016).

3.2. Energy resolution

The energy deposited by the interacting gamma photons was measured as the sum of all the eight digitized position signals.

$$E = X_1^+ + X_1^- + Y_1^+ + Y_1^- + X_2^+ + X_2^- + Y_2^+ + Y_2^- . \quad (3)$$

Energy resolution values were calculated as the ratio of the full width at half maximum (FWHM) to the centroid value of the energy spectrum, expressed as a percentage. The FWHM and centroid values were extracted from Gaussian fits to the 511 keV photopeak of the energy spectra. Three different energy resolutions were calculated: detector level energy resolution, crystal level energy resolution, and crystal-depth level energy resolution.

Detector level energy resolution values were calculated using the data obtained from the flood histograms. A detector-level energy spectrum was generated using events from all crystals in the crystal array. One detector level energy resolution value was obtained for each crystal array at each bias voltage.

Crystal level energy resolution values were also calculated using the data obtained from the flood histograms. However, energy spectra were generated for each crystal after assigning events to each crystal. At each bias voltage, 64 energy resolution values were obtained for each crystal array. The average value and the standard deviation value of the 64 energy resolution values of the detector were used as a measure of the detector crystal level energy resolution.

Crystal-depth level energy resolution were calculated using the data obtained from the DOI resolution measurement and at the optimal bias voltage determined for the flood histogram, which was 55.0 V and 57.0 V for LYSO-based and BGO-based detectors, respectively. Energy spectra were generated for each crystal and at each depth, and energy resolution values were also calculated for each crystal and at each depth. Eight-hundred and ninety-six and 1792 individual energy resolution values were calculated for detectors based on 20 mm thick crystal arrays and 30 mm thick crystal arrays, respectively. The average value and the standard deviation value of all energy resolution values were used as a measure of the detector-depth-level energy resolution.

3.3. Timing resolution

Data for timing resolution was obtained from the same dataset as the flood histogram measurements (figure 3). Most of the crystal pairs from the two detectors in coincidence registered few events, as shown in figure 4, due to the geometry of the system and the source. Hence, only the crystal pairs of $C_i^1 C_{65-i}^2$ were used to evaluate the timing resolution ($i = 1 \ldots 64$ represents the position of the crystal element in the crystal array, and C_i^1 and C_{65-i}^2 are the crystal elements in detectors A and B, respectively).

Timing resolution was calculated for each selected crystal pair of $C_i^1 C_{65-i}^2$. The FWHM of the Gaussian fit to the timing spectrum was obtained for each pair, and the average value for all pairs was used as the measure of the timing resolution of the detector.

3.4. DOI resolution

The DOI resolution was measured using one dual-ended readout detector in coincidence with a reference detector based on a 1 × 16 array of MicroFJ-30035 SiPMs (ON Semiconductors, USA) and a 0.5 × 20 × 50 mm^2 LYSO slab wrapped with Teflon (Yang et al 2019). The reference detector together with the ^{22}Na point source were mounted on a linear stage (model T-LSM100, Zaber Technologies, Canada). The distance of the ^{22}Na point source to the reference detector was 50 mm, and the distance of the ^{22}Na point source to dual-ended readout detector was 20 mm (Yang et al 2019).

DOI data were obtained at nine depths (from 2 to 18 mm, in 2 mm intervals) and 14 depths (from 2 mm to 28 mm, in 2 mm intervals) for the 20 mm and 30 mm crystal arrays, respectively. The bias voltage for the reference detector, LYSO detectors, and BGO detectors were 28.0 V, 55.0 V and 57.0 V, respectively. The bias voltage for the LYSO and BGO detectors were set to their optimal values based on the flood histogram measurements.

The DOI information was calculated using

$$\mathrm{DOI} = a\frac{E_1 - E_2}{E_1 + E_2} + b \tag{4}$$

$$E_1 = X_1^+ + X_1^- + Y_1^+ + Y_1^- \tag{5}$$

$$E_2 = X_2^+ + X_2^- + Y_2^+ + Y_2^- \quad (6)$$

where E_1 (equation 5) and E_2 (equation 6) were the two energies detected by the two SiPM arrays coupled to the two ends of the crystal array and 'a' and 'b' were the fit parameters used to model the DOI and the ratio of the two energies, respectively. Parameters 'a' and 'b' were different for each crystal array and crystal element in the same array (Du et al 2018).

The FWHM of the Gaussian fit to the DOI profile of a crystal at one depth was treated as the DOI resolution of this crystal at this depth. The average DOI resolution value across all depths for a given crystal was treated as the DOI resolution of this crystal, and the average DOI resolution value across all depths and all crystals of one detector was treated as the DOI resolution of the detector.

4. Results

4.1. Flood histogram

The flood histograms obtained at the optimal bias voltages are shown in figure 5, and the flood histogram quality for each detector obtained at different bias voltages are shown in figure 6. Although the flood histograms obtained for the LYSO arrays showed better crystal location accuracy, those obtained using the BGO arrays were able to clearly resolve all the pixels in the array. One can see from figure 6, how the flood histogram quality obtained using the 20 mm BGO crystals was consistently greater than that for 30 mm BGO crystals, with the polished ones doing better than the unpolished of the same thickness.

Figure 6 (bottom) also shows that the optimal bias voltages for the detector based on the LYSO arrays and the BGO arrays are different, 55.0 V and 57.0 V, respectively, which was caused by the different light outputs of the LYSO and BGO crystals.

4.2. Energy resolution

The energy spectra of a corner, edge, and a center crystal in the 20 mm thick LYSO array and the 20 mm thick unpolished BGO array are shown in figure 7. The average energy resolution for the 511 keV photopeak across all the crystal elements (crystal level energy resolution) obtained at different bias voltages is shown in figure 8. For a selected crystal material, the energy resolution obtained using the 20 mm long crystals was better than that obtained using the 30 mm long crystals, and the average energy resolution obtained using the polished BGO arrays was better than these obtained using the unpolished BGO arrays.

Interestingly, the average energy resolution across all crystals (crystal level energy resolution) obtained using the BGO arrays was slightly better than these obtained using the LYSO arrays for a given crystal thickness (figure 8).

The energy spectra of a center crystal in the 20 mm thick LYSO array and the 20 mm thick unpolished BGO array for different DOI depths are shown in figure 9. The 511 keV photopeak positions obtained at different depths were normalized to the value obtained at a depth of 10 mm. The average energy resolution across all crystals obtained at different

depths (crystal-depth level energy resolution), and at the optimal bias voltage for each flood histogram, are shown in figure 10. At each depth, the average energy resolution across all crystals for the LYSO arrays was better than those obtained using the BGO arrays. The average 511 keV photopeak positions across all crystals obtained at different depths are shown in figure 11. The 511 keV photopeak position of the LYSO arrays showed a much larger variation across depth than those of the BGO arrays, which agrees with the data in figure 9 and explains why the crystal level energy resolution for LYSO was relatively poor when depth information was not used.

4.3. Timing resolution

The timing spectra of a corner, edge, and a center crystal in the 20 mm thick LYSO arrays and the 20 mm thick unpolished BGO arrays are shown in figure 12. The peak positions of the timing spectra were crystal dependent. The average timing resolution across all crystals obtained at different bias voltages are shown in figure 13. Better timing resolution was obtained at higher bias voltages for all crystals and thicknesses. Slightly better timing resolution was obtained using the 20 mm BGO crystals compared to the 30 mm BGO crystals. Polished and unpolished BGO crystals showed very similar performance. The timing resolution obtained using the LYSO arrays and the BGO arrays at their corresponding optimal bias voltages for flood histogram were ~1.2 ns and ~5 ns, respectively.

4.4. DOI resolution

The DOI response profiles of one central selected crystal in the 20 mm and 30 mm long crystal arrays are shown in figures 14 and 15, respectively. The response profiles for the crystals with different thicknesses are similar. The polished LYSO array and the unpolished BGO array showed a clear correlation between the DOI response and the DOI position, for each dataset. The DOI resolution of the 20 mm LYSO array and the 20 mm unpolished BGO array were 2.31 ± 0.17 mm and 3.53 ± 0.25 mm, respectively. The polished BGO arrays did not provide DOI information. Average DOI resolutions across all the crystals and all the depths are listed in table 3, and better DOI resolution values were obtained using the LYSO array for a selected crystal thickness.

5. Discussion and conclusions

In this study, dual-ended readout detectors based on BGO arrays with two thicknesses (20 and 30 mm) were compared to LYSO arrays with the same thicknesses. The performance of the detectors obtained at the bias voltages that optimized their flood histograms are summarized in table 4. The inferior performance of BGO-based detectors in terms of flood quality and timing performance compared to LYSO-based detectors was expected due to the lower light yield and slower scintillation properties of BGO (table 1) (Ramirez et al 2005, Du et al 2009). However, all BGO elements were resolved clearly in the crystal array (figure 5) and the energy resolution and 511 keV photopeak positions of the BGO arrays showed less dependence on DOI of the gamma photons (figures 9-11).

The crystal level energy resolutions were ~20–30%, which are not as good as other detectors consisting of LYSO and BGO with similar thickness. The inferior energy resolution was

caused by the dual-ended readout method and the use of the Toray reflector, which decreased the total light collection efficiency in order to make it change with the interaction depth (figures 9 and 10). The energy resolution can be improved significantly if it is depth-corrected (figures 8 and 10, table 4).

The coincidence timing resolution of the BGO detectors was ~5 ns, which are similar to that of the PETbox scanner (Zhang et al 2010), but not as good as the timing resolutions obtained by other researchers (Szczęśniak et al 2013 and González et al 2016b), due to the multiplexing readout method and the dual-ended readout detector design method. Better timing resolution can be obtained by extracting the timing information from each SiPM individually, however, the cost of the readout electronics will be increased significantly. Cherenkov photons also have been proposed to improve the timing resolution of BGO-based PET detectors (Brunner and Schaart 2017, Kwon et al 2019), however, due to the very low yield of Cherenkov photons, it is difficult to design multi-channel low-noise readout electronics to work with practical BGO-based TOF-PET detectors.

An interesting finding is that dual-ended readout detectors based on polished BGO arrays and Toray reflector did not provide any DOI information. In contrast, our previous studies (Du et al 2018, 2019a, 2019b), replicated again here, showed that same combination with LYSO does provide good DOI resolution (figures 14 and 15). That difference could be potentially explained by a combination of the greater index of refraction of BGO (2.15) compared to LYSO (1.82) and of the polished surface treatment that makes the photons bounce inside the crystal several times before reaching the photodetector (Janecek and Moses 2008), thus losing their correlation with the interaction point of the gamma photon. The DOI resolution of BGO-based detectors could likely be improved using reflectors with higher absorption, such as black paint absorber, however, the flood histogram, energy resolution, and timing resolution would get worse. Further studies would be needed to confirm these hypotheses and have a better understanding of the effect of surface treatment and reflector choice on DOI resolution with BGO crystals.

In our studies, the crystals originated from different sources and the crystal arrays were fabricated by different manufacturers, however, we think this had a negligible effect on the results shown in this paper. Both LYSO and BGO are mature crystals and similar crystal polishing methods and array fabrication methods were used.

In conclusion, dual-ended readout detectors based on an unpolished BGO array with Toray reflector are good candidates for non-TOF pre-clinical PET scanners aimed at low-activity dynamic studies such as cell tracking (Bao and Chatziioannou 2010, Freedenberg et al 2014, Ouyang et al 2016). Higher detection efficiency and lower cost when compared to LYSO, also can make such BGO-based detectors an attractive option for low-cost organ-dedicated human systems, such as brain imagers for imaging low-affinity neuroreceptor ligands, or neuroreceptors with low density.

Acknowledgments

This work was funded by NIH grant R01 EB019439 and R01 EB028806. Junwei Du would like to thank Dr. Stanislaw Majewski for helping with revising the text.

References

Akamatsu G et al. 2019 Performance evaluation of a whole-body prototype PET scanner with four-layer detectors Phys. Med. Biol 64 095014 [PubMed: 30978704]

Bao Q and Chatziioannou A 2010 Estimation of the minimum detectable activity of preclinical PET imaging systems with an analytical method Med. Phys 37 6070–83 [PubMed: 21158319]

Brunner S and Schaart D 2017 BGO as a hybrid scintillator/Cherenkov radiator for cost-effective time-of-flight PET Phys. Med. Biol 62 4421–39 [PubMed: 28358722]

Cherry S, Jones T, Karp J, Qi J, Moses W and Badawi R 2018 Total-body PET: maximizing sensitivity to create new opportunities for clinical research and patient care J. Nucl. Med 59 3–12 [PubMed: 28935835]

Conti M and Bendriem B 2019 The new opportunities for high time resolution clinical TOF PET Clin Transl. Imag 7 139–47

de Marcillac P, Coron N, Dambier G, Leblanc J and Moalic J 2003 Experimental detection of [alpha]-particles from the radioactive decay of natural bismuth Nature 422 876–8 [PubMed: 12712201]

Du J, Bai X and Cherry S 2019a Performance comparison of depth-encoding detectors based on dual-ended readout and different SiPMs for high-resolution PET applications Phys. Med. Biol 64 15NT03

Du J, Bai X, Gola A, Acerbi F, Ferri A, Piemonte C, Yang Y and Cherry S 2018 Performance of a high-resolution depth-encoding PET detector module using linearly-graded SiPM arrays Phys. Med. Biol 63 035035 [PubMed: 29324437]

Du J, Bai X, Liu C, Qi J and Cherry SR 2019b Design and evaluation of gapless curved scintillator arrays for simultaneous high-resolution and high-sensitivity brain PET Phys. Med. Biol 64 235004 [PubMed: 31618708]

Du J, Wang Y, Zhang L, Zhou Z, Xu Z and Wang X 2009 Physical properties of LYSO scintillator for NN-PET detectors Proc. 2009 2nd Int. Conf. on Biomedical Engineering and Informatics 1 314–8

Du J, Yang Y, Bai X, Judenhofer M, Berg E, Di K, Buckley S, Jackson C and Cherry S 2016 Characterization of large-area SiPM array for PET applications IEEE Trans. Nucl. Sci 63 8–16 [PubMed: 27182077]

Freedenberg M, Badawi R, Tarantal A and Cherry S 2014 Performance and limitations of positron emission tomography (PET) scanners for imaging very low activity sources Phys. Medica 30 104–10

González A et al. 2016a A PET design based on SiPM and monolithic LYSO crystals: performance evaluation IEEE Trans. Nucl. Sci 63 2471–7

González A, Sanchez F, Majewski S, Parkhurst P, Vaigneur K and Benlloch JM 2016b Pilot studies with BGO scintillators coupled to low-noise, large-area, SiPM arrays IEEE Trans. Nucl. Sci 63 2482–6

Gsell W et al. 2020 Characterization of a preclinical PET insert in a 7 Tesla MRI scanner: beyond NEMA testing Phys. Med. Biol 54 5155–72

Gundacker S, Acerbi F, Auffray E, Ferri A, Gola A, Nemallapudi MV, Paternoster G, Piemonte C and Lecoq P 2016 State of the art timing in TOF-PET detectors with L(Y)SO scintillators of various sizes coupled to FBK-SiPMs JINST 11 P08008

Ito M, Lee JS, Kwon SI, Lee GS, Hong B, Lee KS, Sim K-S, Lee SJ, Rhee JT and Hong SJ 2010 A four-layer DOI detector with a relative offset for use in an animal PET system IEEE Trans. Nucl. Sci 57 976–81

Janecek M and Moses W 2008 Measuring light reflectance of BGO crystal surfaces IEEE Trans. Nucl. Sci 55 2443–9

Kuang Z et al. 2018 Performance of a depth encoding PET detector module using light sharing and single-ended readout with SiPMs Phys. Med. Biol 64 085012

Kwon S, Roncali E, Gola A, Paternoster G, Piemonte C and Cherry SR 2019 Dual-ended readout of bismuth germanate to improve timing resolution in time-of-flight PET Phys. Med. Biol 64 105007 [PubMed: 30978713]

Müller F, Schug D, Hallen P, Grahe J and Schulz V 2019 A Novel DOI positioning algorithm for monolithic scintillator crystals in PET based on gradient tree boosting IEEE Trans. Radiat. Plasma Med. Sci 3 465–74

Ouyang Y, Kim T and Pratx G 2016 Evaluation of a BGO-based PET system for single-cell tracking performance by simulation and phantom studies Mol. Imag 15 1–8

Pizzichemi M et al. 2019 On light sharing TOF-PET modules with depth of interaction and 157 ps FWHM coincidence time resolution Phys. Med. Biol 64 155008 [PubMed: 31239430]

Ramirez R et al. 2005 A comparison of BGO, GSO, MLS, LGSO, LYSO and LSO scintillation materials for high-spatial-resolution animal PET detectors IEEE Nuclear Science Symp. Conf. Record pp 2835–9

Ren S, Yang Y and Cherry S 2014 Effects of reflector and crystal surface on the performance of a depth-encoding PET detector with dual-ended readout Med. Phys 41 072503 [PubMed: 24989406]

Saint-Gobain 2014 BGO bismuth germanate scintillation material (http://www.crystals.saint-gobain.com)

Saint-Gobain 2017 LYSO scintillation material (http://www.crystals.saint-gobain.com)

Shao Y, Cherry S, Siegel S and Silverman R 1996 A study of inter-crystal scatter in small scintillator arrays designed for high resolution PET imaging IEEE Trans Nucl. Sci 43 1938–44

Shao Y, Sun X, Lan K, Bircher C, Lou K and Deng Z 2014 Development of a prototype PET scanner with depth-of-interaction measurement using solid state photomultiplier arrays and parallel readout electronics Phys. Med. Biol 59 1223–38 [PubMed: 24556629]

Son J, Lee M and Lee J 2017 A depth-of-interaction PET detector using a stair-shaped reflector arrangement and a single-ended scintillation light readout Phys. Med. Biol 62 465–83 [PubMed: 28000613]

St James S, Yang Y, Bowen S, Qi J and Cherry S 2014 Simulation study of spatial resolution and sensitivity for the tapered depth of interaction PET detectors for small animal imaging Phys. Med. Biol 55 N63–N74

Szczęśniak T, Kapusta M, Moszynski M, Grodzicka M, Szawlowski M, Wolski D, Baszak J and Zhang N 2013 MPPC arrays in PET detectors with LSO and BGO scintillators IEEE Trans. Nucl. Sci 60 1533–40

Watanabe M, Saito A, Isobe T, Ote K, Yamada R, Moriya T and Omura T 2017 Performance evaluation of a high-resolution brain PET scanner using four-layer MPPC DOI detectors Phys. Med. Biol 62 7148–66 [PubMed: 28753133]

Yamamoto S, Watabe H, Watabe T, Ikeda H, Kanai Y, Ogata Y, Kato K and Hatazawa J 2016 Development of ultrahigh resolution Si-PM based PET system using 0.32 mm pixel scintillators Nucl. Instrum. Methods Phys. Res. A 836 7–12

Yang Q, Kuang Z, Sang Z, Yang Y and Du J 2019 Performance comparison of two signal multiplexing readouts for SiPM-based PET detector Phys. Med. Biol 64 23NT02

Yang Y et al. 2016 A prototype high-resolution small-animal PET scanner dedicated to mouse brain imaging J. Nucl. Med 57 1130–5 [PubMed: 27013696]

Zhang H, Vu NT, Bao Q, Silverman RW, Berry-Pusey BN, Douraghy A, Williams DA, Rannou FR, Stout DB and Chatziioannou AF 2010 Performance characteristics of BGO detectors for a low cost preclinical PET scanner IEEE Trans. Nucl. Sci 57 1038–44 [PubMed: 21165154]

Zhang Y, Yan H, Baghaei H and Wong W-H 2016 A novel depth-of-interaction block detector for positron emission tomography using a dichotomous orthogonal symmetry decoding concept Phys. Med. Biol 61 1608–33 [PubMed: 26836144]

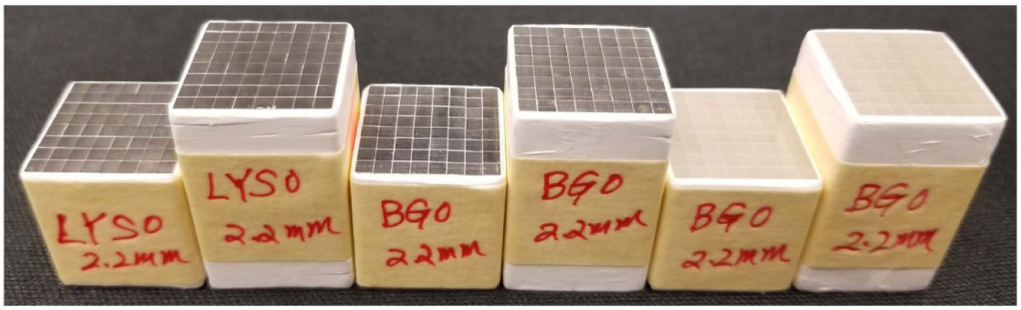

Figure 1.

Picture of (from left to right) polished LYSO arrays with pixel thickness of 20 mm and 30 mm, polished BGO arrays with pixel thickness of 20 mm and 30 mm, and unpolished BGO arrays with a thickness of 20 mm and 30 mm. The pitch sizes of the crystal arrays were all 2.2 mm.

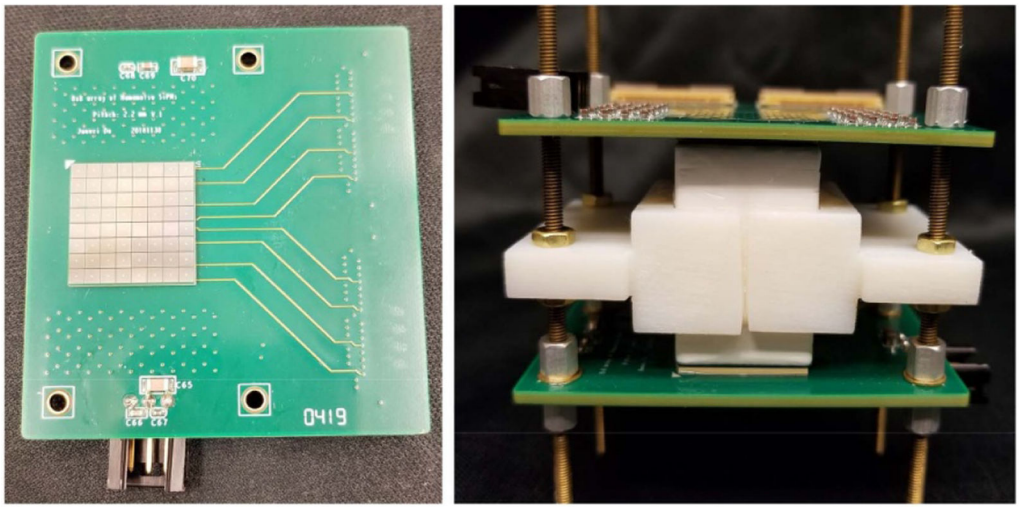

Figure 2.
Pictures of (left) a Hamamatsu 13361-2050-08 SiPM array mounted on a printed circuit board and (right) a complete dual-ended readout detector assembly.

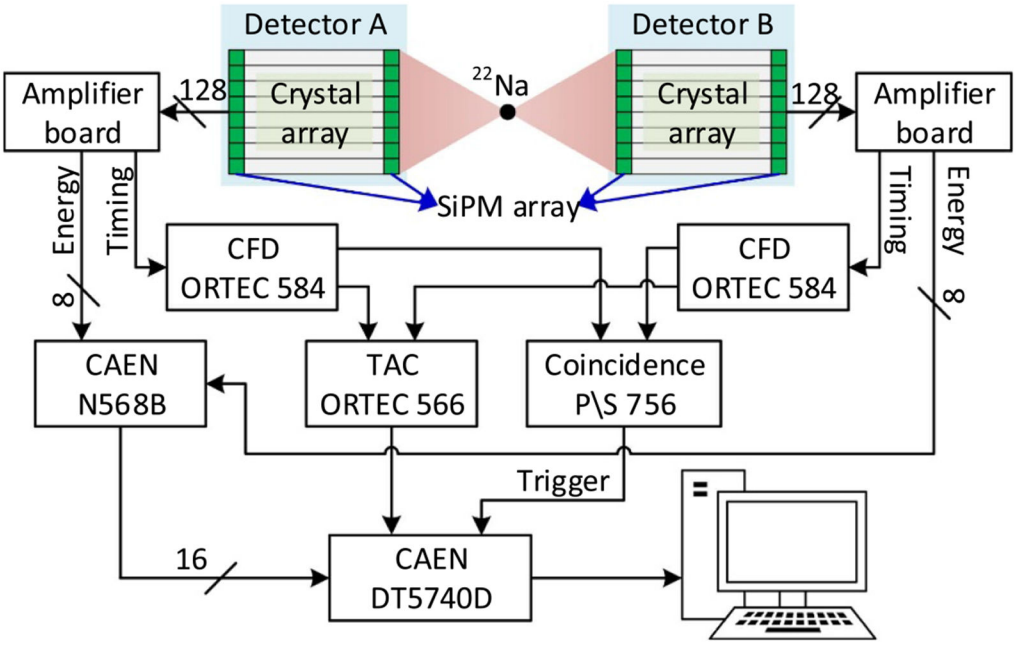

Figure 3.

Schematic diagram of the experimental setup with readout electronics for flood histogram and timing measurements. Detector B was replaced by a reference detector in DOI measurement.

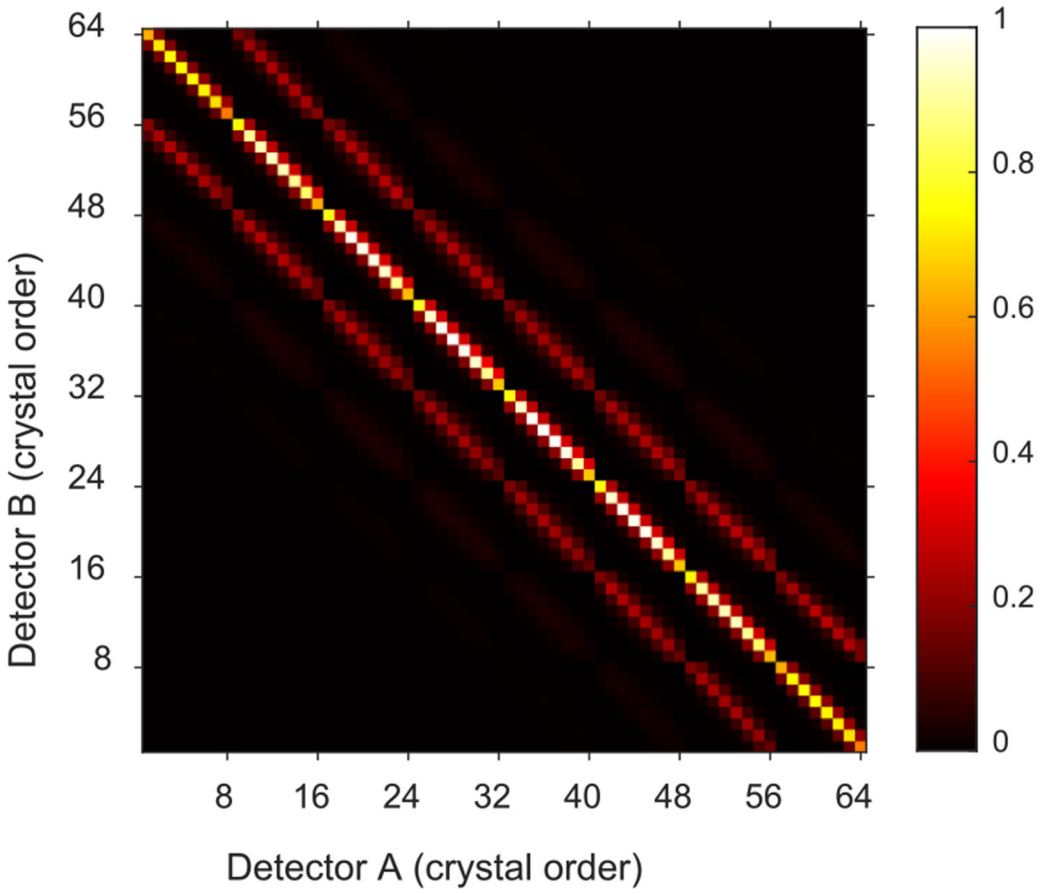

Figure 4.

Example of normalized counts obtained for each crystal pair, using the detectors based on polished BGO array with a thickness of 20 mm and a point source. The crystal pairs along the diagonal which had significant number of events were used to calculate the coincidence timing resolution.

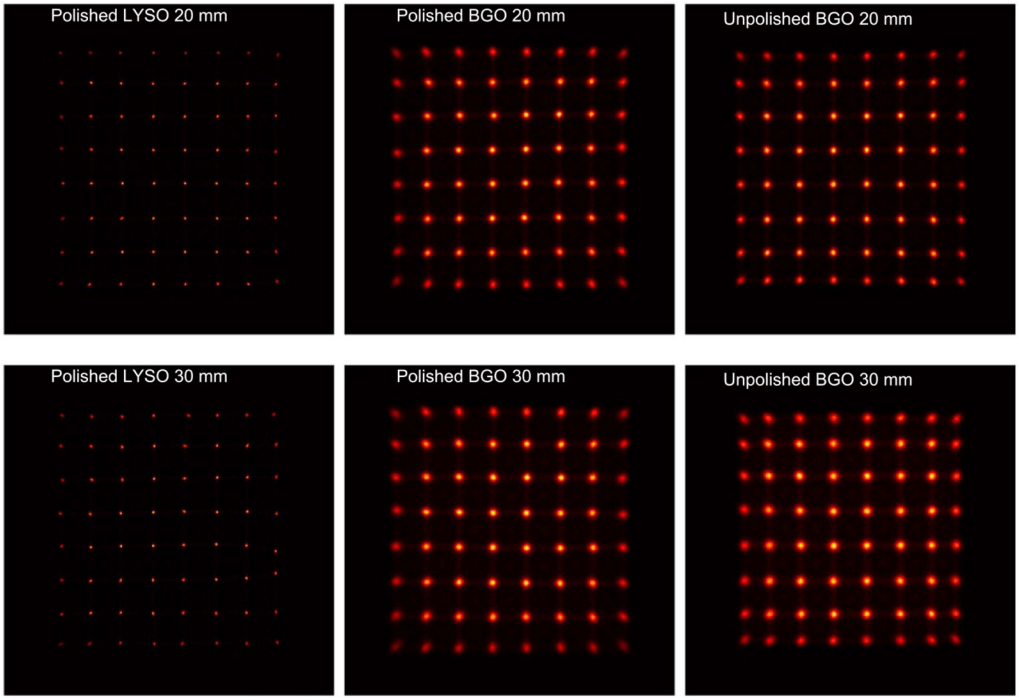

Figure 5.
Flood histograms obtained using different crystal arrays.

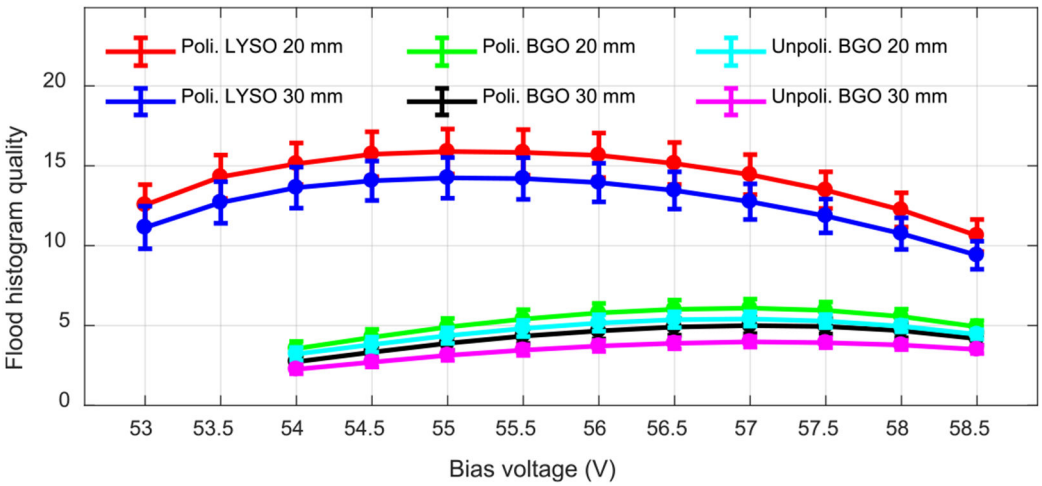

Figure 6.

Flood histogram quality versus bias voltage. The error bars are the standard deviation of the flood quality metric across all crystals.

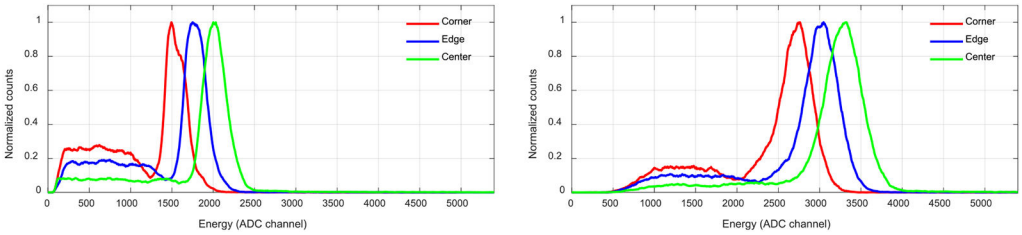

Figure 7.

Crystal level energy spectra of three crystals, obtained using (left) LYSO array with a thickness of 20 mm and a bias voltage of 55.0 V, and (right) unpolished BGO array with a thickness of 20 mm and a bias voltage of 57.0 V. To use the full range of the digitizer, the gains of the signal were different for detectors based on the LYSO arrays and BGO arrays.

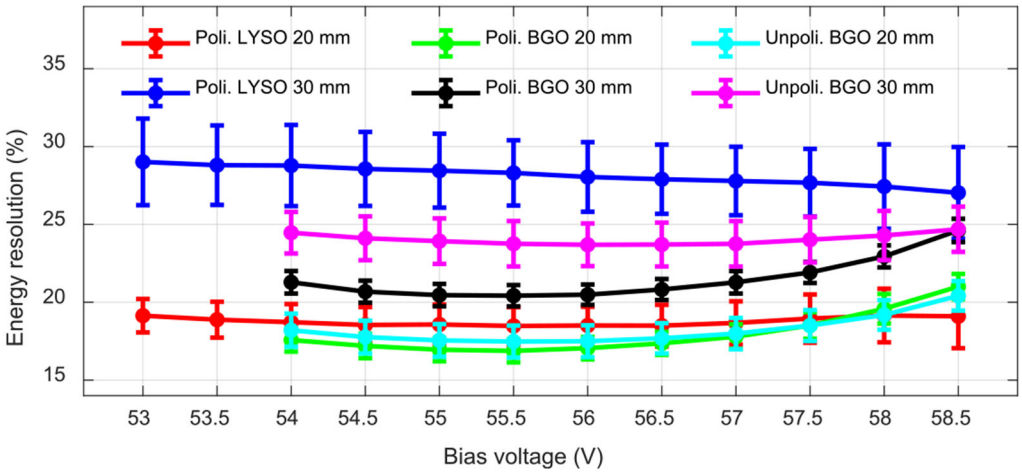

Figure 8.

Average crystal level energy resolution versus bias voltage. The error bars are the standard deviation value of energy resolution across all crystals.

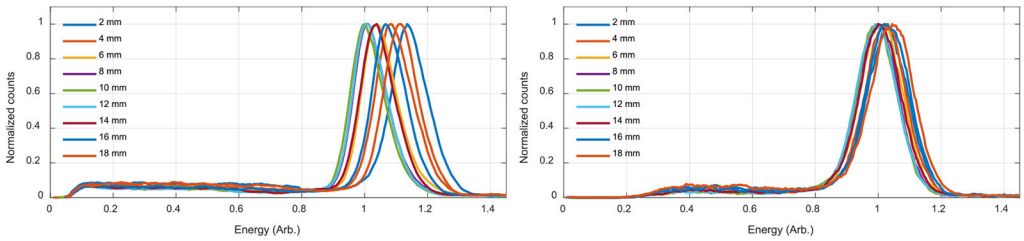

Figure 9.

Energy spectra of a center crystal obtained at different depths for (left) LYSO array with a thickness of 20 mm and a bias voltage of 55.0 V, and (right) unpolished BGO array with a thickness of 20 mm and a bias voltage of 57.0 V. The photopeak positions are normalized to that obtained at a depth of 10 mm.

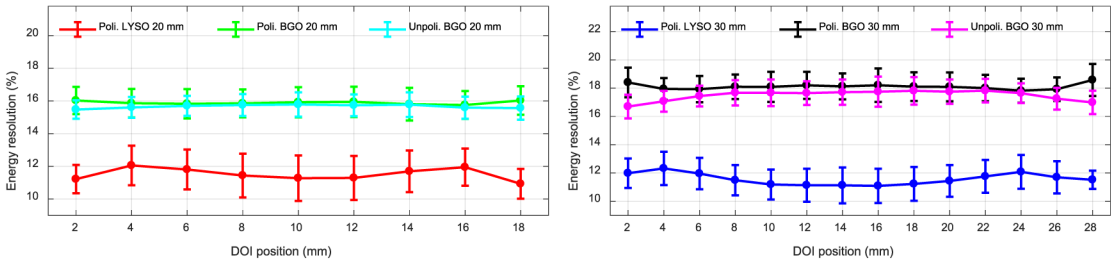

Figure 10.

Average crystal-depth level energy resolution versus depth. The error bars are the standard deviation value of energy resolution across all depths.

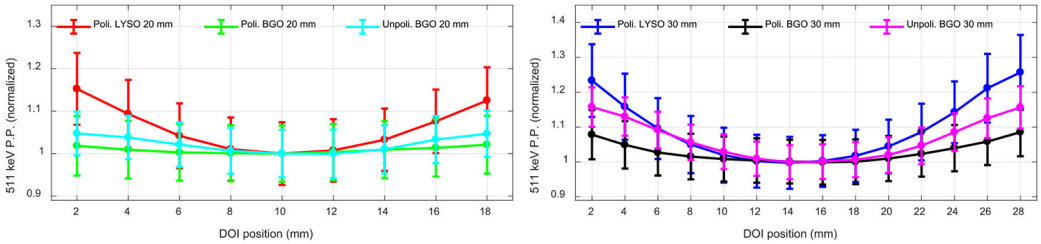

Figure 11.

511 keV photopeak position versus depth. The photopeak position was normalized to the value obtained at the middle of the crystal arrays. The error bars are the standard deviation of the 511 keV photopeak positions across all crystals.

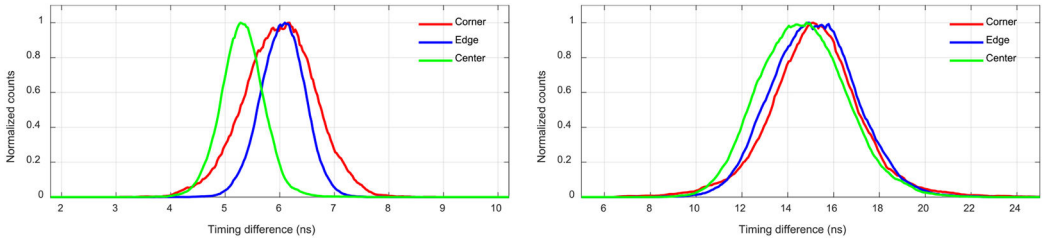

Figure 12.

Timing spectra of three crystals, obtained using (left) LYSO array with a thickness of 20 mm and a bias voltage of 55.0 V, and (right) unpolished BGO array with a thickness of 20 mm and a bias voltage of 57.0 V.

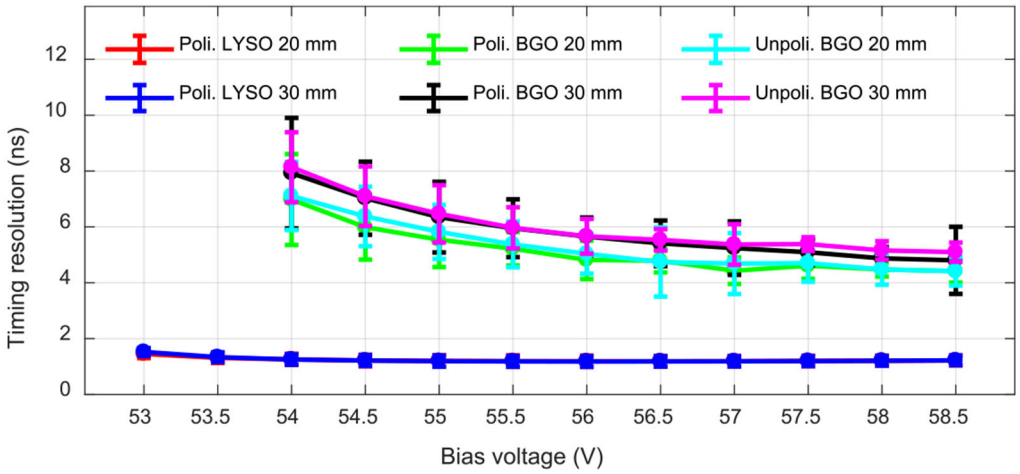

Figure 13.

Average timing resolution versus bias voltage. The error bars are the standard deviation value of timing resolution across all crystals.

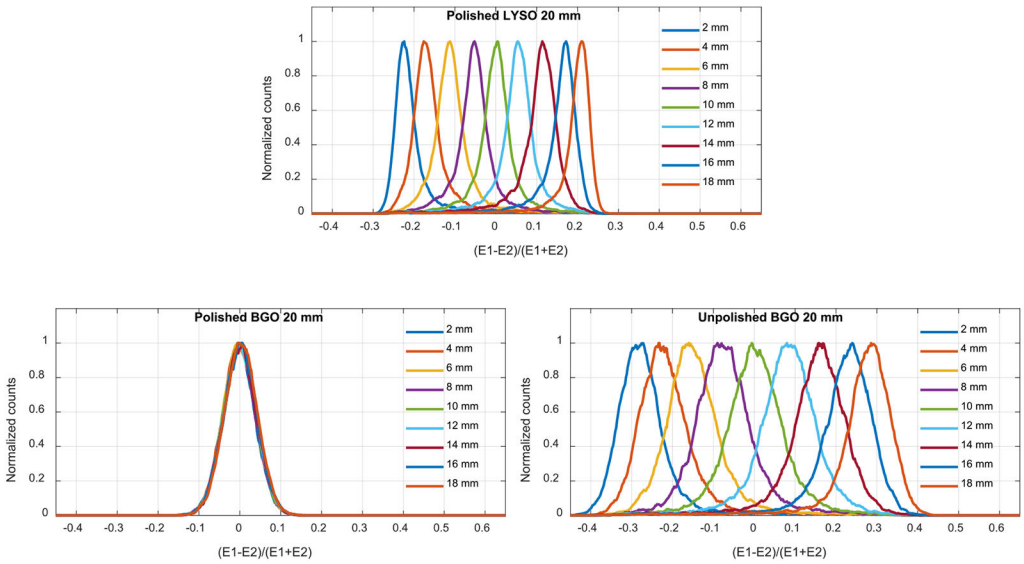

Figure 14.

DOI response profiles of one central crystal in the 20 mm long polished LYSO array (top), 20 mm polished BGO array (bottom left) and 20 mm unpolished BGO array (bottom right).

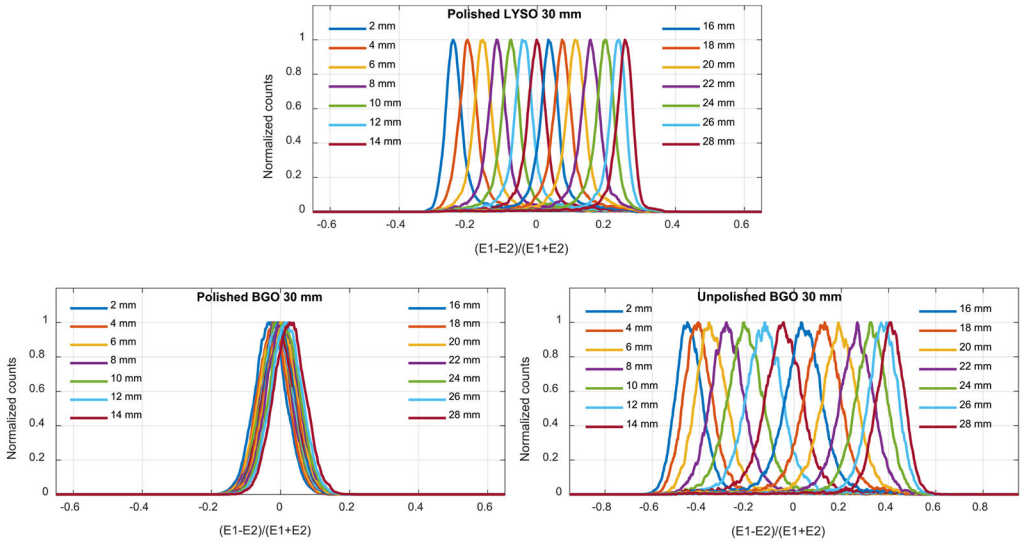

Figure 15.

DOI response profiles of one central crystal in the 30 mm long polished LYSO array (top), 30 mm polished BGO array (bottom left) and 30 mm unpolished BGO array (bottom right).

Table 1.

Properties of LYSO and BGO (from Saint-Gobain 2014, 2017).

	LYSO	BGO
Effective atomic number (Z_{eff})	60	74
Density (g cm^{-3})	7.1	7.13
Attenuation length for 511 keV (cm)	1.2	1.0
Light yield (photons MeV^{-1})	8000–10 000	30 000
Decay time (ns)	37–45 ns	300
Peak wavelength (nm)	420	480

Table 2.

Crystal array origins and surface treatments.

	Surface treatment[a]	Crystal source	Crystal array manufacturer
Polished LYSO arrays	All crystal surfaces polished.	Crystal Photonics Inc. Florida, USA	Crystal Photonics Inc. Florida, USA
Polished BGO arrays	All crystal surfaces polished.	Nikolaev Institute of Inorganic Chemistry, Novosibirsk, Russia	Crystal Photonics Inc. Florida, USA
Unpolished BGO arrays	Four lateral sides of the crystals unpolished, two ends polished.	Shanghai Institute of Ceramics, Shanghai, China	Sichuan Tianle Photonics Co., Ltd, Sichuan, China

[a]All the polished surfaces were machine polished.

Table 3.

DOI resolution for each crystal array.

	Crystal thickness	
Crystal array	**20 mm**	**30 mm**
Polished LYSO array	2.31 ± 0.17 mm	2.95 ± 0.32 mm
Polished BGO array	No DOI	No DOI
Unpolished BGO array	3.53 ± 0.25 mm	4.35 ± 0.39 mm

Table 4.

Performance summary of three dual-ended readout detectors.

		Polished LYSO		Polished BGO		Unpolished BGO	
		20 mm	**30 mm**	**20 mm**	**30 mm**	**20 mm**	**30 mm**
Optimal bias voltage for flood histogram (V)		55.0	55.0	57.0	57.0	57.0	57.0
Flood histogram quality		15.8 ± 1.4	14.2 ± 1.3	6.1 ± 0.6	5.0 ± 0.5	5.4 ± 0.5	4.0 ± 0.3
Energy resolution (%)	Detector	24.8 ± 0.1	33.5 ± 0.3	22.8 ± 0.1	24.3 ± 0.1	23.1 ± 0.1	27.7 ± 0.1
	Crystal	18.6 ± 1.3	28.5 ± 2.4	17.8 ± 0.8	21.3 ± 0.7	18.0 ± 1.0	23.8 ± 1.5
	Crystal-depth	11.5 ± 1.2	11.6 ± 1.2	15.8 ± 0.9	18.1 ± 1.0	15.7 ± 0.7	17.5 ± 0.9
DOI resolution (mm)		2.31 ± 0.17	2.95 ± 0.32	No DOI	No DOI	3.53 ± 0.25	4.35 ± 0.39
Timing resolution (ns)		1.19 ± 0.20	1.20 ± 0.21	4.43 ± 0.47	5.24 ± 0.96	4.68 ± 1.0	5.37 ± 0.73